JOURNAL OF GEOPHYSICAL RESEARCH, VOL. 117, A06222, doi:10.1029/2012JA017537, 2012

A case study of proton precipitation at Mars: Mars Express observations and hybrid simulations

C. Diéval,[1,2] E. Kallio,[3] S. Barabash,[1] G. Stenberg,[1] H. Nilsson,[1] Y. Futaana,[1] M. Holmström,[1] A. Fedorov,[4] R. A. Frahm,[5] R. Jarvinen,[3] and D. A. Brain[6]

Received 17 January 2012; revised 2 May 2012; accepted 4 May 2012; published 16 June 2012.

[1] Using the data from the Analyzer of Space Plasma and Energetic Atoms (ASPERA-3) experiment on board Mars Express and hybrid simulations, we have investigated the entry of protons into the Martian induced magnetosphere. We discuss one orbit on the dayside with observations of significant proton fluxes at altitudes down to 260 km on 27 February 2004. The protons observed below the induced magnetosphere boundary at an altitude of less than 700 km have energies of a few keV, travel downward, and precipitate onto the atmosphere. The measured energy flux and particle flux are 10^8–10^9 eV cm^{-2} s^{-1} and 10^5–10^6 H$^+$ cm^{-2} s^{-1}, respectively. The proton precipitation occurs because the Martian magnetosheath is small with respect to the heated proton gyroradius in the subsolar region. The data suggest that the precipitation is not permanent but may occur when there are transient increases in the magnetosheath proton temperature. The higher-energy protons penetrate deeper because of their larger gyroradii. The proton entry into the induced magnetosphere is simulated using a hybrid code. A simulation using a fast solar wind as input can reproduce the high energies of the observed precipitating protons. The model shows that the precipitating protons originate from both the solar wind and the planetary exosphere. The precipitation extends over a few thousand kilometers along the orbit of the spacecraft. The proton precipitation does not necessarily correlate with the crustal magnetic anomalies.

Citation: Diéval, C., et al. (2012), A case study of proton precipitation at Mars: Mars Express observations and hybrid simulations, *J. Geophys. Res.*, *117*, A06222, doi:10.1029/2012JA017537.

1. Introduction

[2] When the supersonic solar wind carrying the interplanetary magnetic field (IMF) flows around a planet such as Mars, which is surrounded by an ionosphere but lacks a global magnetic field, it induces currents in the ionosphere. The associated magnetic field deflects the solar wind flow and results in the formation of an obstacle, the induced magnetosphere. A bow shock and a magnetosheath are also formed similarly to the conventional magnetosphere. The IMF drapes around the conductive ionosphere on the dayside of the planet, and it is stretched into a magnetotail on the nightside. The draping configuration results from the superposition of the IMF and the magnetic field of the currents induced in the ionosphere. The stretched magnetotail results from mass loading of the magnetic field tubes moving in the upper parts of the ionosphere. If the obstacle was perfectly non-conductive neither draping nor stretching would have occurred. The region of the field draping is called the magnetic pile-up region. It is roughly limited at the upper edge by the induced magnetosphere boundary (IMB), where pressure balance is achieved between the solar wind dynamic pressure and the magnetic pressure [e.g., *Dubinin et al.*, 2008]. At the IMB, the ion composition of the plasma changes from proton-dominated to heavy-ion dominated. The lower boundary of the magnetic pile-up region, referred to as the photoelectron boundary (PEB), is characterized by the appearance of the CO_2 photoelectrons [*Frahm et al.*, 2006] and a sharp increase in the electron number density [*Dubinin et al.*, 2008]. The picture of the Martian magnetosphere is further complicated by the presence of strong crustal magnetic field anomalies in the Southern hemisphere [*Acuña et al.*, 1998, 1999]. Further details of the solar wind interaction with Mars can be found in the review by *Nagy et al.* [2004].

[3] The IMB envelops the solar wind void but is not impenetrable. Due to the small size of the induced magnetosphere, particularly in the subsolar region, the effect of a finite gyroradius becomes important, and the shocked solar

[1]Swedish Institute of Space Physics, Kiruna, Sweden.
[2]Also at Division of Space Technology, Department of Computer Science, Electrical and Space Engineering, Luleå Technical University, Kiruna, Sweden.
[3]Finnish Meteorological Institute, Helsinki, Finland.
[4]Institut de Recherche en Astrophysique et Planetologie, Toulouse, France.
[5]Southwest Research Institute, San Antonio, Texas, USA.
[6]Laboratory for Atmospheric and Space Physics, University of Colorado, Boulder, Colorado, USA.

Corresponding author: C. Diéval, Swedish Institute of Space Physics, Box 812, SE-98128, Kiruna, Sweden. (catherine@irf.se)

wind protons may penetrate through the IMB and precipitate onto the Martian ionosphere. This paper uses data analysis and hybrid modeling to study how the protons penetrate into the ionosphere.

[4] Proton precipitation on Mars has previously been studied by two global hybrid models. In the first model, *Brecht* [1997] simulated the direct impact of the solar wind H^+ ions at the surface of Mars and showed that the rate of deposition of precipitating protons depends on the solar wind dynamic pressure and the angle of the IMF with respect to the solar wind velocity. The energy flux, which is deposited in the upper atmosphere by the precipitating protons, varies spatially, and is controlled by the solar wind convection electric field $\vec{E}_{sw} = -\vec{v}_{sw} \times \vec{B}$, where $\vec{B}$ is the IMF vector and $\vec{v}_{sw}$ is the solar wind velocity vector. In the second model, *Kallio and Janhunen* [2001] studied the solar wind H^+ ion precipitation onto the Martian atmosphere and the related effects on the atmospheric neutrals. They showed that on the dayside, the hemisphere aligned with the convection electric field experiences a higher energy flux of precipitating protons than the opposite hemisphere; and the energy flux is also higher at low solar zenith angle (SZA) than at high SZA.

[5] Some direct and indirect observations are also available. *Lundin et al.* [2004] reported that solar wind protons can reach altitudes as low as 270 km. They used the in situ plasma data of the Analyzer of Space Plasma and Energetic Atoms (ASPERA-3) experiment on board the Mars Express (MEX) mission. The penetration of solar wind alpha particles into the ionosphere of Mars was demonstrated by *Stenberg et al.* [2011]. The entry of the solar wind electrons into the Martian atmosphere has also been studied extensively [see, e.g., *Brain et al.*, 2005; *Fränz et al.*, 2006].

[6] This paper provides ASPERA-3 measurements of energy/particle fluxes of the downward-moving protons into the Martian atmosphere in the subsolar region and proposes a mechanism to explain the proton precipitation. The paper also investigates the origin of the proton fluxes using hybrid modeling, and suggests that the precipitation is a transient phenomenon. Section 2 presents the instruments that provide the data used in this study. Section 3 describes the observations of proton precipitation fluxes. In section 4, the hybrid code used in this study and the modeling results are briefly presented. Finally, the results are discussed in section 5.

2. Instrumentation

[7] ASPERA-3 is an instrument package designed to study the interaction between the solar wind and the Martian atmosphere [*Barabash et al.*, 2006]. It comprises the Electron Spectrometer (ELS), the Ion Mass Analyzer (IMA) and two energetic neutral atom sensors.

[8] For this study, the ELS instrument measures the two-dimensional distributions of the electron flux in the energy range 5 eV–15 keV ($\Delta E/E = 8\%$) with a field of view (FOV) of $4^\circ \times 360^\circ$ divided into 16 azimuth sectors. The time resolution used in this study is 4 s. Observation of very low-energy electrons is prohibited by a repelling grid voltage of −5 V.

[9] The IMA instrument consists of an electrostatic deflection system followed by a top-hat electrostatic energy analyzer and a magnetic mass analyzer. The IMA sensor measures the fluxes of different ion species with m/q resolution (m and q are the ion mass and charge, respectively) in the energy range of 200 eV/q–36 keV/q. The measured ions include H^+, He^{2+}, O^+ and molecular ions with $20 < m/q < 80$. With a time resolution of 12 s, IMA gives a two-dimensional measurement of the ion fluxes (16 azimuth sectors) for all energies. Electrostatic sweeping provides ±45° coverage out of the plane of the aperture, and a complete distribution with a FOV of $90^\circ \times 360^\circ$ is produced in 192 s (one elevation scan).

[10] Both ELS and IMA have other operational modes that are not used in this paper.

3. Observations

[11] We present a detailed analysis of one event from the subsolar region (within 0–45° SZA) where the proton fluxes are observed below the IMB. The event is recorded by Mars Express/ASPERA-3 on 27 February 2004 (orbit 154). This orbit was chosen because the protons were observed during several consecutive IMA scans down to the pericenter and because the protons had energies up to 7 keV. The present paper contains a deeper analysis of the proton penetration reported by *Lundin et al.* [2004], which briefly considered the same orbit.

[12] Figure 1 presents the data from the event. Figure 1a shows the altitude and the SZA of the spacecraft, and Figure 1b shows the magnitude and the angle of the crustal magnetic field vector relative to the local zenith. The magnetic field vector is derived at the spacecraft position from the Cain model [*Cain et al.*, 2003]. Figure 1c shows the electron energy-time spectrogram (averaged over sectors 4–8).

[13] The pass through the dayside ionosphere is visible in the electron data as a thin horizontal, the so-called photoelectron line, at ∼20 eV. These electrons are produced by photoionization of the atmospheric CO_2 [*Frahm et al.*, 2006]. The pericenter altitude of ∼260 km is reached at ∼19:40 UT. The outbound crossings of the photoelectron boundary (PEB) at ∼19:46:30 UT and the induced magnetosphere boundary (IMB) at ∼19:47:30 UT are indicated with vertical lines. The decrease of the high-energy electron flux (>80 eV) is used to identify the inbound IMB crossing. The disappearance of the ionospheric electrons indicates that MEX made an incursion into the magnetosheath between ∼19:25:30 UT and 19:27:00 UT. At that time, MEX had an altitude of 900–1000 km near the terminator. The inward motion of IMB and the appearance of the magnetosheath plasma likely result from a pulse of increased solar wind dynamic pressure which occurred between 19:25:30 UT and 19:27:00 UT, pushing the shocked electrons closer to Mars.

[14] Figure 1c shows that the high-energy electron flux (with energy up to 400 eV) gradually decreases from 19:27 UT until 19:41 UT as MEX approaches the planet. The electron entries are intermittent. Similar entries of high-energy electrons were previously observed by ASPERA-3 [e.g., *Lundin et al.*, 2004; *Soobiah et al.*, 2006] and the Mars Global Surveyor (MGS) electron reflectometer [e.g., *Mitchell et al.*, 2001]. The flux of shocked electrons is decreased compared to the flux in the magnetosheath proper and becomes less energetic. Furthermore, the photoelectrons become more visible when the magnetosheath flux weakens. The intermittent penetration of shocked electrons may be

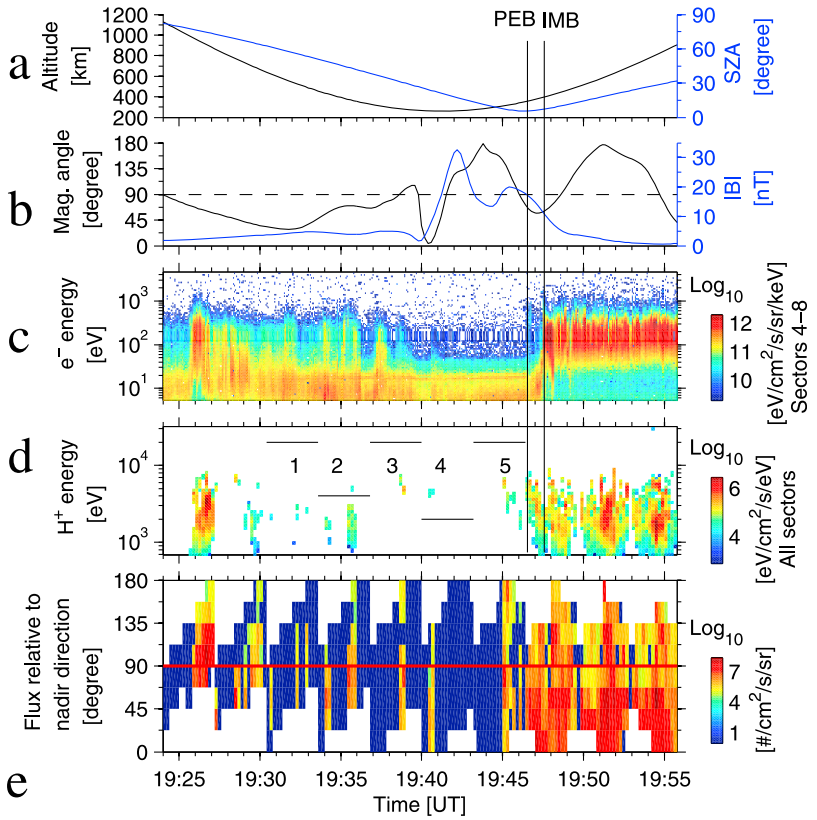

Figure 1. Observations made on 27 February 2004 (19:24 UT–19:56 UT). (a) Altitude (left axis, black solid curve) and solar zenith angle (SZA) (right axis, blue solid curve). (b) Magnitude of the crustal magnetic field (right axis, blue solid curve) and angle of the crustal magnetic field vector relative to the local zenith from the Cain model (left axis, black solid curve) at the spacecraft position. The direction of the modeled magnetic field vector is shown relative to the zenith. Hence, 0° and 180° correspond to the locally upward and downward vertical magnetic fields, respectively; 90° corresponds to a locally horizontal magnetic field. (c) Electron energy-time spectrogram averaged over the azimuth sectors 4–8. The unit is $\log_{10}$(eV cm^{-2} s^{-1} sr^{-1} keV^{-1}). (d) Proton energy-time spectrogram averaged over all azimuth sectors. The unit is $\log_{10}$(eV cm^{-2} s^{-1} eV^{-1}). (e) Observed direction of the proton fluxes relative to nadir for the energy range 1.1–10.5 keV. The unit is $\log_{10}$(H^{+} cm^{-2} s^{-1} sr^{-1}). Hence, 0° and 180° correspond to the fluxes directed toward the nadir and the zenith, respectively. A horizontal solid red line is drawn at 90° to separate the downgoing flux (below the line) from the upgoing flux (above the line). The black vertical solid lines indicate the plasma boundaries.

caused by the rapid and small-amplitude back-and-forth motions of the IMB above MEX while MEX is located in the magnetic pile-up region. Note, however, that MEX is always below the IMB during this period. Between 19:41 UT and 19:46 UT, the spacecraft is located in the ionosphere and no sheath electron entries are observed.

[15] The protons are shown in Figures 1d and 1e. Figure 1d shows the proton energy-time spectrogram (averaged over all azimuth sectors) and Figure 1e presents the direction of the observed proton fluxes relative to nadir, binned in 22.5° bins. In Figure 1d, only the fluxes above the (one-count) background level are shown. Each time interval of 12 s corresponds to measurements at a fixed elevation angle over 360° azimuths. After 12 s, the voltage settings of the deflector system are changed to measure at the next elevation angle. In 192 s, we observe 16 different elevations (a full elevation scan), giving a coverage of ±45 degrees out of the plane of the aperture. The "blob" shape of the proton flux is due to this elevation sweep. Each elevation scan of interest is given a number and is indicated by a horizontal solid line in Figure 1d. The white areas in Figure 1e are the directions not covered by the measurement or the directions blocked by the spacecraft. The flux in Figure 1e is integrated over the energy range 1.1–10.5 keV.

[16] There are five elevation scans with significant proton fluxes (compared to the background level) at altitudes below 700 km: 19:31–19:33 UT (scan 1), 19:34–19:36 UT (2), 19:38–19:39 UT (3), 19:40–19:41 UT (4) and 19:45–19:46 UT (5). The proton flux in scans 1 to 5 drops by a factor of ~10–100 compared to the values in the magnetosheath. We notice that the protons are accompanied by shocked electrons, between 19:27 UT and 19:41 UT (including scans 1–4), while we see protons without shocked electrons in scan 5. The protons are relatively abundant below the IMB during the inbound pass (scans 1–4), and only sporadic fluxes are seen during the outbound pass (scan 5). The orbit

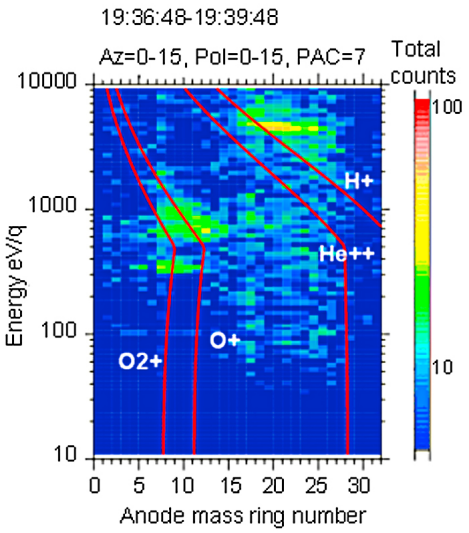

Figure 2. Plasma composition during scan 3. The ion fluxes are shown as a function of energy and radial position on the Ion Mass Analyzer (IMA) detection plate. The skewed red lines are curves of constant m/q for H^+, He^{2+}, O^+ and O_2^+. The counts shown are integrated over all azimuth sectors and all elevations.

geometry during the inbound pass is such that MEX skims the IMB; therefore the orbit geometry is favorable to an extended period where protons are observed below the IMB. On the outbound pass, the orbit geometry is different and we observe a narrow region of proton precipitation (scan 5) and a sharp IMB crossing (at ~19:47:30 UT). Within one given scan, the protons are not continuously observed, which might be because the looking directions of the instrument do not match the proton flux.

[17] From Figure 1e, we find that on average, 81% of the total proton particle flux (total = upward + downward) measured during these 5 scans is moving downward (angle to nadir < 90°), and it can be considered as a precipitating flux. The protons below the IMB flow both toward and away from Mars, and the angle distribution is broad, covering several angular bins within a downgoing hemisphere.

[18] However we cannot be sure that the protons will actually reach the exobase (the measurements are made down to only 260 km in altitude). The exobase altitude is ~180 km at solar minimum. Regardless, we assume that this event shows a clear case of proton precipitation.

[19] Mars Express does not carry a magnetometer: to relate the observed precipitation event to the crustal magnetic field, we use the Cain model [*Cain et al.*, 2003]. We note that the magnetic field predicted by the Cain model is not likely the field experienced by MEX because the draped induced magnetic field, which is typically ≥30 nT at low SZA, is expected to dominate [*Brain et al.*, 2005]. In Figure 1b, we see that the spacecraft is passing above weak crustal field regions |B| < 35 nT and that the magnetic zenith angle varies between different proton flux observations. For comparison, the magnitude of the draped magnetic field in the subsolar region during this orbit is ~50 nT [*Brain et al.*, 2005]. Downgoing proton fluxes are observed regardless of the crustal magnetic field direction: horizontal (scan 3), vertical (scans 1 and 4), or intermediate (scans 2 and 5). The crustal magnetic field strength is >10 T during 19:41 UT–19:47 UT, while proton fluxes are still sporadically detected during this period. Therefore, we argue that neither the orientation nor the strength of the crustal field influence the proton precipitation in the ionosphere.

[20] Figure 2 shows the plasma composition of scan 3. The ion fluxes are presented as a function of the energy and the radial position on the detection plate in the IMA detector. The red lines are curves of constant m/q corresponding to H^+, He^{2+}, O^+ and O_2^+. The counts shown are integrated over all azimuth sectors and all elevations, during ~3 min.

[21] In this study heavy planetary ions (O^+, O_2^+) were recorded during scans 1, 3, 4 and 5. However, before May 2007, the instrumental energy cut–off for heavy ions was 200 eV [*Lundin et al.*, 2008], which explains why the heavy ions are not detected during all scans. Additionally, alpha particles were only observed during scan 2. The protons can sometimes be observed together with the alpha particles at low altitudes [*Stenberg et al.*, 2011].

[22] To verify our assumption that the proton fluxes have a magnetosheath origin, in Figure 3, we plot the energy spectrum of the scans 1–5 together with a magnetosheath energy spectrum from the same orbit (taken at SZA ~20°).

[23] The black vertical dashed line indicates the instrumental energy cutoff for the respective mode of IMA, and the blue dashed line represents the one-count level. Due to the decrease of the detection efficiency with the energy,

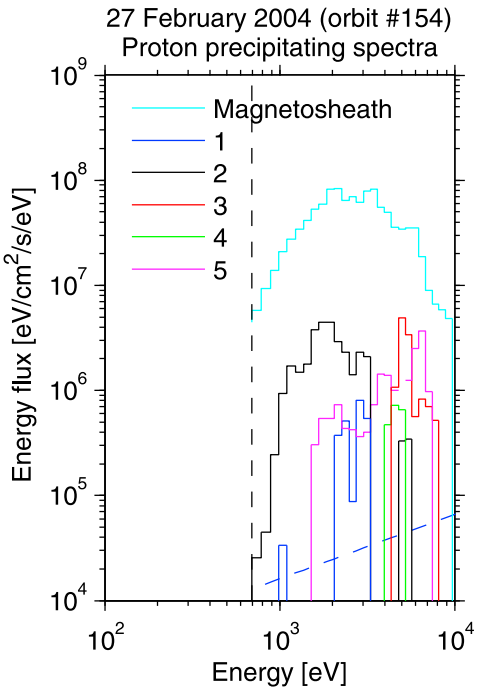

Figure 3. Energy flux of precipitating protons for scans 1–5. A magnetosheath energy spectrum obtained during the same orbit is also shown. The unit is eV cm^{-2} s^{-1} eV^{-1}. See text for details.

which is an inherent feature of the IMA detector geometry, the fluxes corresponding to the one-count level increase with the energy. However, the observed fluxes are well above the one-count level for the shown energy range.

[24] The maximum magnetosheath flux is approximately 2 orders of magnitude higher than the maximum precipitating proton flux. The magnetosheath energy spectrum peaks at ~2 keV, which indicates that the upstream solar wind must be fast and may explain the observation of protons with energies up to 7 keV close to Mars during the investigated period. Overall, the proton fluxes recorded below the IMB are not more energetic than the magnetosheath protons. The hypothesis of a magnetosheath origin of the penetrating protons is further examined in section 4.

[25] All scans with recorded proton fluxes that are discussed in the paper are summarized in Table 1. The energy range and the peak energy of the proton energy spectra are given with an indicator of whether the shocked electrons were observed during the scan. The table gives the spacecraft altitude, the SZA, the crustal magnetic field magnitude and the crustal magnetic zenith angle for each scan. In the table, the maximum values of the energy flux ($7{\cdot}10^9$ eV cm^{-2} s^{-1}) and the particle flux ($3{\cdot}10^6$ H$^+$ cm^{-2} s^{-1}) are shown in boldface. In summary, the precipitating proton fluxes of 10^5–10^6 H$^+$ cm^{-2} s^{-1} (and energy fluxes of 10^8–10^9 eV cm^{-2} s^{-1}) are observed in the altitude range of ~260–630 km for SZA between 7°–60°. The precipitating protons seem unrelated to the location and the topology of the crustal magnetic fields.

[26] In order to investigate effects of the different upstream conditions, we used the MGS proxy defined by *Crider et al.* [2003] to derive the solar wind dynamic pressure, and we used the MGS magnetic field data to derive the IMF direction following the approach described by *Fedorov et al.* [2006]. The upstream dynamic pressure proxy value was nominal: 0.99 nPa (close to the average value = 1.06 nPa [*Crider et al.*, 2003]). This value may not represent the sudden pulse of increased dynamic pressure (19:25:30 UT–19:27:00 UT), but it may correspond to a period of more quiet solar wind conditions following the increased pressure pulse. Nevertheless, the IMB crossing with altitude of ~393 km at 7° SZA at 19:47:30 UT is lower than average. This suggests that the overall solar wind dynamic pressure remains high during our observations. Thus, we believe that the case of proton precipitation presented here is associated with high dynamic pressure conditions.

[27] In MSO (Mars Solar Orbital) coordinates, the y and z components of the IMF are estimated to be [−1.6, −2.5] nT for the analyzed case. In MSO, the *x* axis points from the center of Mars toward the Sun, the z axis points toward the orbital north and the *y* axis completes the right hand system. Assuming a Parker spiral shape for the IMF, we conclude that the IMF points dawnward and the solar wind convection electric field points southward. The hybrid modeling studies [*Brecht*, 1997; *Kallio and Janhunen*, 2001] predict that the proton precipitation would be more intensive in the hemisphere where $\vec{E}_{sw}$ points away from the planet. In our case, this hemisphere is the southern hemisphere, where the proton precipitation is indeed observed. However, no further conclusion could be drawn without a statistical study.

[28] In section 4, we use hybrid modeling to interpret the observational data. The input to the model is the upstream IMF that we just discussed.

4. Hybrid Simulations

[29] We use the HYB-Mars model, a 3-D quasi-neutral hybrid model, and we will compare the modeling results with the observations of proton precipitation found on 27 February 2004. The HYB–Mars model is described in detail by *Kallio et al.* [2010] and the references therein. Here, we briefly discuss the fundamental parts of the model and the new features added since the work by *Kallio et al.* [2010].

[30] HYB-Mars is a particle-in-cloud model [*Kallio and Janhunen*, 2003]. The plasma ions are treated as macroparticles, which correspond to groups of real plasma ions, and the electrons are treated as a massless charge-neutralizing fluid. The code includes finite gyroradius effects, which makes it suitable to study ion precipitation.

[31] The ions are accelerated by the Lorentz force:

$$m_i \frac{d\vec{v}_i}{dt} = q_i\left(\vec{E} + \vec{v}_i \times \vec{B}\right) \tag{1}$$

where $\vec{E}$ and $\vec{B}$ are the electric field and the magnetic field, and m_i, $\vec{v}_i$ and q_i are the mass, velocity and electric charge of an ion *i*, respectively. The electric field is calculated from the electron momentum equation:

$$\vec{E} = -\vec{U}_e \times \vec{B} - \frac{\vec{\nabla}(n_e k T_e)}{e n_e} \tag{2}$$

where k is the Boltzmann's constant, e is the unit electron charge, and n_e, T_e and $\vec{U}_e$ are the electron density, temperature and bulk velocity, respectively. The gradient term in equation (2) is the electron gradient pressure, which is also called the ambipolar electric field.

[32] The model uses the MSO Cartesian coordinate system. The aberration angle of the solar wind direction, caused by the Martian orbital motion, is neglected in this study. The size of the simulation box is $-4.2\ R_m < x, y, z < 4.2\ R_m$, where $R_m = 3393$ km is the radius of Mars. In the simulation, the grid size depends on the distance, r, from the center of Mars: the grid size is 720 km where $r > 3\ R_m$, 360 km where $2\ R_m < r < 3\ R_m$ and 180 km where $r < 2\ R_m$. The observations were made at $r < 1.32 R_m$. The total running time was 585 s with a time step of 0.02 s. The average number of ions per cell is significant: ~30. The model does not include the crustal magnetic anomalies.

[33] The model contains two spherically symmetric exospheres (oxygen and hydrogen) surrounding Mars. They are sources of H$^+$ and O$^+$ ions. We use the models of the respective coronae adopted by the Solar Wind Interaction with Mars (SWIM) modeling comparison team [see *Brain et al.*, 2010].

[34] The hydrogen neutral profile used is

$$n\left(H\left[m^{-3}\right]\right) = N_1 \cdot \exp(A_1 \cdot (1/R_1 - 1/r)) + N_2 \cdot \exp(A_2 \cdot (1/R_2 - 1/r)) \tag{3}$$

where $N_1 = 1.5{\cdot}10^{11}$, $N_2 = 1.9{\cdot}10^{10}$, $A_1 = -25965{\cdot}10^3$, $A_2 = -10365{\cdot}10^3$, $R_1 = 3593.5{\cdot}10^3$, $R_2 = 3593.5{\cdot}10^3$, r is the distance from the center of Mars (in meters) and the indices

Table 1. Summary of Proton Precipitation Fluxes[a]

Scans, 27 February 2004	Energy Range (keV)	Energy Peak (keV)	Shocked Electrons	Altitude (km)	Solar Zenith Angle (°)	Crustal B (nT)	Magnetic Zenith Angle (°)	Particle Flux (cm^{-2} s^{-1})	Energy Flux (eV cm^{-2} s^{-1})
1	1.–4.	2.5	yes	627	61.7	3.7	32	$2{\cdot}10^5$	$6{\cdot}10^8$
2	1.–4.	2.	yes	437	49.4	4.5	54	$\mathbf{3{\cdot}10^6}$	$6{\cdot}10^9$
3	4.–7.	5.	yes	281	30.7	4.6	94	$1{\cdot}10^6$	$6{\cdot}10^9$
4	4.5–5.	5.	yes	262	23.5	7.8	7	$2{\cdot}10^5$	$8{\cdot}10^8$
5	1.5–7.	7.	no	310	7.6	17.8	149	$2{\cdot}10^6$	$\mathbf{7{\cdot}10^9}$

[a]Boldface indicates the maximum values of the energy flux ($7{\cdot}10^9$ eV cm^{-2} s^{-1}) and the particle flux ($3{\cdot}10^6$ H^+ cm^{-2} s^{-1}).

1 and 2 refer to the thermal and hot hydrogen profiles, respectively. The thermal component is taken from *Chaufray et al.* [2008]. We take the photoionization rate as $5.58{\cdot}10^{-8}$ s^{-1}, which is also used by *Ma et al.* [2004] and *Fulle et al.* [2007].

[35] The neutral hot oxygen profile is modeled as

$$n\left(O\left[m^{-3}\right]\right) = N_1 \cdot \exp(-(r-R_0)/B_1) + N_2 \cdot \exp(-(r-R_0)/B_2) + N_3 \cdot \exp(-(r-R_0)/B_3) \quad (4)$$

where $N_1 = 5.23{\cdot}10^9$, $N_2 = 9.76{\cdot}10^8$, $N_3 = 3.71{\cdot}10^{10}$, $B_1 = 626.2{\cdot}10^3$, $B_2 = 2790{\cdot}10^3$, $B_3 = 88.47{\cdot}10^3$, $R_0 = 3393.5{\cdot}10^3$, and r is the distance from the center of Mars (in meters). We take the photoionization rate as $8.89{\cdot}10^{-8}$ s^{-1}, which is also used by *Ma et al.* [2004]. The values of the density and the photoionization rates for the neutral profiles correspond to the solar minimum conditions.

[36] The ionosphere is not self-consistently modeled. O^+ and O_2^+ ions are emitted from the inner boundary of the model. The inner boundary is a spherical shell at 207 km altitude, which mimics the exobase. The emission of ionospheric oxygen ions is proportional to $0.1 + 0.9{\cdot}\cos(SZA)$ on the dayside, and it is constant (0.1) on the nightside [*Kallio et al.*, 2010].

[37] The hybrid model implements the electron impact ionization reactions, and the charge-exchange (CX) reactions between the planetary atoms and the planetary/solar wind protons. Details of the reactions are given by *Kallio et al.* [2010].

[38] In our model, the solar wind contains protons and alpha particles. We have conducted two simulations with different input parameters. For both simulations, we use a solar wind density of 2.5 cm^{-3} (the nominal value at Earth scaled to the heliocentric distance of Mars) and a solar wind temperature of $1.5{\cdot}10^5$ K. In both simulations, the IMF vector is chosen as [0, −1.6, −2.5] nT. The y and z components were estimated from the MGS data (see section 3). For simplicity, the x component has been assumed to be zero, which means that the IMF is perpendicular to the Mars-Sun line. The simulations differ only by the solar wind velocity. The simulations, called "nominal SW" and "fast SW," use a solar wind velocity of 487 km^{-1} and 1028 km^{-1}, respectively. Theses values correspond to dynamic pressures of 1.0 nPa and 4.4 nPa, respectively. The solar wind velocity is taken opposite to the x axis in both simulations.

[39] Two different dynamic pressure values are used to look at the precipitation dynamics. The "fast SW" simulation corresponds to the observations on 27 February 2004 (proton energy up to 7 keV in Figure 1d) being discussed here. We chose the upstream solar wind velocity for the "fast SW" run somewhat arbitrary just requiring that the energy peak of the input upstream solar wind must be larger than that of the measured magnetosheath energy spectrum (cyan curve in Figure 3). Note that the angular separation between Mars and the Earth during the time of observations was too great (77°) to allow a reliable extrapolation of the solar wind conditions from the WIND or ACE spacecraft.

[40] The code uses an absorbing boundary condition for the ions on the inner boundary. An ion is removed from the simulation if it hits this boundary. In reality, the ions would not be immediately neutralized, but they would be scattered via the collisions with the atmospheric neutrals [*Kallio and Barabash*, 2001, Figure 2].

[41] In this study, we consider two proton populations: the solar wind protons and the exospheric protons. The exospheric protons originate from the hydrogen corona and include photoions, protons created by electron impact ionization and protons created by the CX reactions between the planetary neutral hydrogen and the protons of solar wind/planetary origin. To compare the observations with the simulations, we place a virtual tube detector of radius 170 km along the spacecraft orbit. During 435 s, the position $\vec{r}_i$, the velocity $\vec{v}_i$, and the weight w_i of an ion i are recorded when the ion enters the tube detector at the time t_i. The ion weight tells the number of real ions to which a macroparticle corresponds. The radius of the tube detector is on the order of the smallest cell size. This type of detector allows one to make simulated energy time spectrograms along the orbit [*Kallio et al.*, 2008]. The collected ions are binned logarithmically in 52 energy steps from 0.1 to 32 keV using the IMA energy table. The tube detector is divided into small cylindrical elements, where the length of a segment is equal to the distance covered by the spacecraft during 12 s. Hence, the length corresponds to the IMA time resolution for a 2-D measurement at a fixed elevation. We have used the surface of each cylindrical element (the wall of the cylinder) as the collecting surface for the particles. The FOV of a cylindrical element is 360° × 180°. The wall of each cylindrical element is divided into 16 individual azimuth sectors. The proton flux is calculated relative to the normal vector to the surface of each azimuth sector and summed up over all sectors. Figure 4 shows a cylindrical element of the tube detector, together with the velocity vector of an ion hitting the element, the normal vector to an azimuth sector, and a segment along the orbit (thick line).

[42] The particle flux (in units of H^+ cm^{-2} s^{-1} eV^{-1}) through a cylindrical surface element of radius R and length L is given by the following:

$$F = \frac{1}{2 \cdot \pi \cdot R \cdot L \cdot \Delta t} \sum_{i,j,k} \frac{w_k \cdot \cos\left(\alpha_{jk}\right)}{\Delta E_i} \quad (5)$$

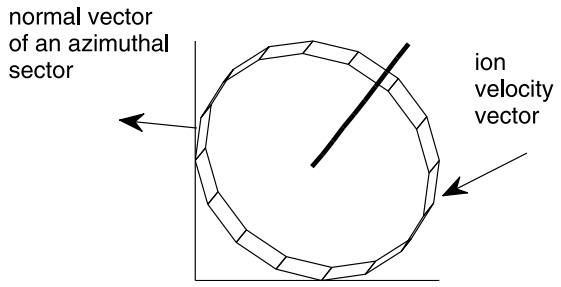

Figure 4. Schema of a cylindrical element of the tube detector, divided into 16 azimuth sectors. The velocity vector of an ion hitting the element, the normal vector of an azimuth sector, and a segment along the orbit (the thick line) are also shown.

where α_{jk} is the angle between the velocity of an ion k and the normal vector of an azimuth sector j and w_k is the weight of an ion k recorded at the energy step E_i of width ΔE_i in the azimuth sector j.

[43] The central plane of the FOV of the cylindrical element always points perpendicular to the velocity vector of the spacecraft, which gives an ideal orientation to detect particles coming from different directions relative to the local nadir. However, the simulated energy-time spectrograms are not meant to be compared in great detail with the data but to give a qualitative picture of the simulated proton distributions along the orbit.

[44] Figure 5 presents the simulated energy-time spectrograms from the tube detector and compares them with the observations. Shown are the "fast SW" simulation and the "nominal SW" simulation. In both simulations, we distinguish between the planetary protons (Figures 5b and 5g) and the solar wind protons (Figures 5c and 5h). Figures 5d and 5i include all protons. Figures 5a and 5f have the same format as Figure 1a. Figures 5e and 5j have the same format as Figure 1d. The simulated energy-time spectrograms show the first "entry point" of the ions into the tube (each ion can enter the tube several times while gyrating).

[45] The simulations (Figures 5d and 5i) indicate that the proton flux is significant at high altitudes, which is

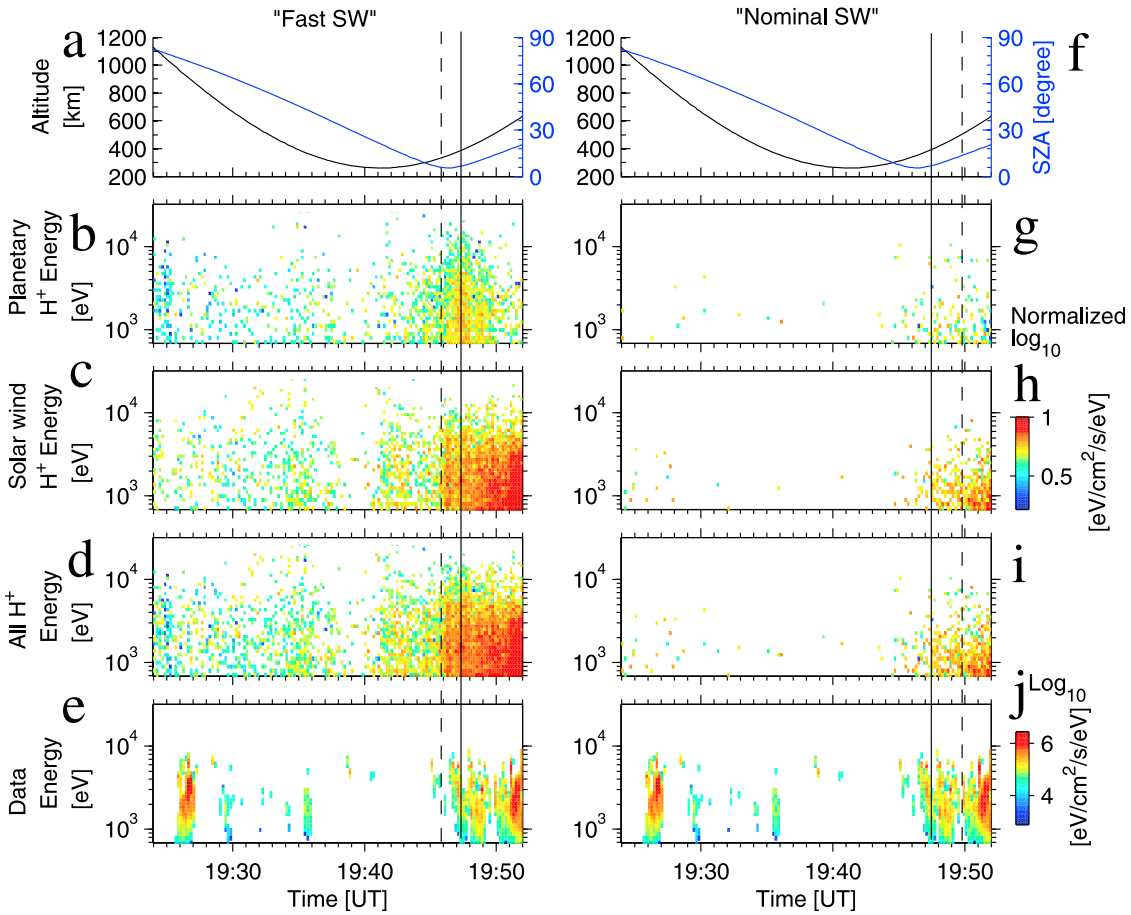

Figure 5. Results from the "fast SW" simulation and the "nominal SW" simulation. (a and f) Same format as Figure 1a. Simulated energy-time spectrogram for (b and g) the planetary protons, (c and h) the solar wind protons and (d and i) all proton populations. In each simulated spectrogram, the unit is $\log_{10}$(eV cm^{-2} s^{-1} eV^{-1}), normalized to the maximum value from Figure 5d. (e and j) Data (Figure 1d) reprinted for ease of comparison. In the simulation, we use a field of view (FOV) of 4π sr, but the FOV of the IMA instrument is narrower. The induced magnetosphere boundary (IMB) crossings determined from observations and from simulations are shown by a vertical solid line and a dashed line, respectively.

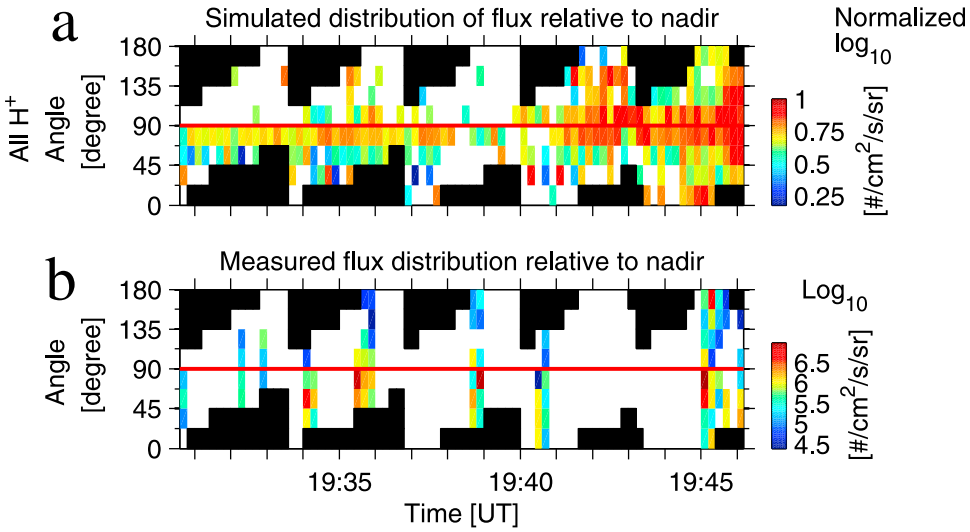

Figure 6. (a) Simulated distribution of flux directions relative to the nadir for all proton populations in the "fast SW" simulation. The flux in units of $\log_{10}(H^+ \text{ cm}^{-2} \text{ s}^{-1} \text{ sr}^{-1})$ is normalized to the maximum value, and the white color indicates no particles. (b) Distribution of flux directions relative to nadir, in the same format as Figure 1e; the white color indicates no flux. The black shaded area shows angles excluded from IMA's field of view.

consistent with the observations (Figures 5e and 5j). However, both simulations indicate that the proton flux is the lowest near the pericenter, whereas the observations show that the proton flux is still significant. The simulations also indicate both low- and high-energy particles near the pericenter, whereas there are only protons with energies above 4 keV in the IMA data there. These two issues will be examined further in section 5. When comparing the two simulations, there are more proton entries in the "fast SW" run than in the "nominal SW" run. Assuming that the magnetic pressure balances the solar wind dynamic pressure in the pile-up region ($v^2 \sim B^2$), we get $v \sim B$ and thus the gyroradius ($\sim v/B$) may not change much between the two runs. On the other hand, the pile-up region gets more compressed in the "fast SW" run, and becomes a smaller obstacle to the heated proton.

[46] The vertical solid line in Figure 5 indicates the time of the measured IMB crossing. The vertical dashed line indicates the time of a plasma boundary crossing in the simulation (we call it IMB crossing). In the "fast SW" simulation, there is a sharp IMB crossing at ~19:46 UT at ~339 km altitude. In the "nominal SW" simulation, there is a smooth IMB crossing at ~19:50 UT at ~516 km altitude. Thus, the sharp low-altitude IMB crossing of the high dynamic pressure case matches the measured IMB crossing (19:47:30 UT at ~393 km altitude) better than the IMB crossing of the nominal pressure case does. The "fast SW" simulation indicates a significant proton flux below the IMB crossing, while the "nominal SW" simulation shows significantly less particles penetrating the IMB. The "fast SW" simulation reproduces the high proton flux before 19:41 UT, as seen in the data, while the "nominal SW" simulation does not. On the other hand, the "fast SW" simulation overestimates the flux between 19:41 UT and 19:45 UT. This disagreement may be due to the low spatial resolution of the model (180 km size grid at low altitudes).

[47] Naturally the protons entering the induced magnetosphere in the "fast SW" run have higher energies than in the "nominal SW" run. The high solar wind speed also leads to a more efficient acceleration by $\vec{E}_{sw} = -\vec{v}_{sw} \times \vec{B}$. The proton energy in the "nominal SW" simulation is too low compared to the observations, while the "fast SW" simulation can reproduce the high energies of the observed protons.

[48] The model permits to distinguish between planetary and solar wind protons. Comparing the protons of planetary and solar wind origins, we see that according to the model both populations are present below the IMB. We have integrated the particle flux of protons (total = upward + downward) over the energy range shown in Figure 5 and the period 19:24 UT–19:46 UT (interval in the ionosphere). We have done so for each proton population separately. For the "fast SW" simulation, 73% of the total proton flux below the IMB has a solar wind origin. For the "nominal SW" simulation, this number is 63%. The exospheric protons account for the rest. Therefore, the most important contribution comes from the shocked solar wind protons (Figures 5c and 5h). The high-energy planetary protons seen in Figures 5b and 5g are picked up and accelerated by the convection electric field.

[49] Figure 6 shows the simulated distribution of the flux direction relative to the nadir for all proton populations recorded in the tube detector, from the "fast SW" simulation (Figure 6a). The time interval is from 19:30 UT to 19:46 UT, which corresponds to the scans 1–5. The flowing directions of the particles are binned in 22.5° bins, and the flux in each bin is integrated over the energy range 1.1–10.5 keV. The observed flux distribution is shown in Figure 6b, which has the same format as Figure 1e, except that the bins with no flux are shown in white. A horizontal solid red line is drawn at 90° in both plots to separate the downgoing flux (below the line) from the upgoing flux (above the line).

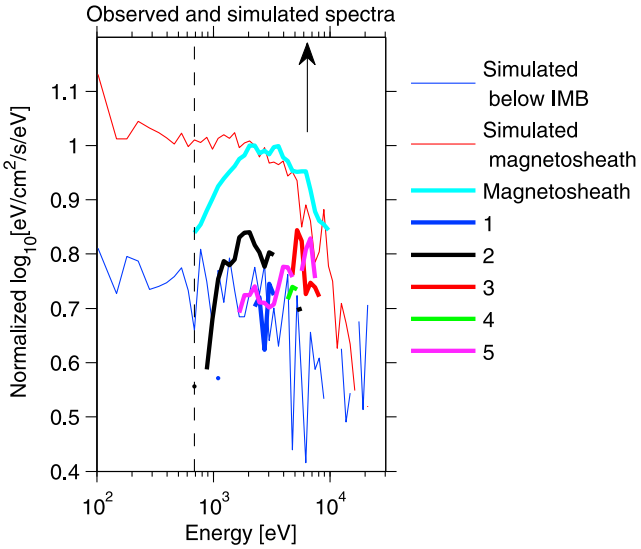

Figure 7. Comparison of the observed energy spectra of precipitating protons (scans 1–5 and magnetosheath, shown as thick lines) with the simulated energy spectra of magnetosheath protons (thin red line) and precipitating protons below the IMB (thin blue line). The vertical dashed black line shows the energy cutoff of IMA. For all energy spectra, the decimal logarithm of the flux (unit: eV cm^{-2} s^{-1} eV^{-1}) is normalized, so that the height of the simulated magnetosheath energy spectrum at ~2 keV is equal to the height of the measured magnetosheath energy spectrum. The arrow indicates the energy peak (5.5 keV) of the simulated upstream solar wind energy spectrum (a Maxwellian distribution).

[50] The simulated angular distribution peaks at 90° relative to the nadir, which means that the flow is mainly horizontal relative to Mars. The simulated distribution also indicates that more particles move downward (precipitating) than upward between 19:30 UT and 19:41 UT, which is in reasonable agreement with the observations. After 19:41 UT, the agreement is worse. On average 87% of the measured total proton flux is moving downward during 19:30 UT–19:41 UT (angle to nadir < 90°). By comparison, if we do the same calculation for the simulated flux (not including the black area in Figure 6b), we find that 79% of the simulated total flux is downward, which agrees reasonably with the data. This result suggests that the absorbing inner boundary can mimic reasonably well the analyzed case. Finally, the model qualitatively confirms that proton precipitation can indeed occur at low altitudes on a large spatial scale. This issue is discussed further in section 5.

[51] Figure 7 shows the observed energy spectra of precipitating protons for scans 1–5 and a magnetosheath energy spectrum (with the same format as in Figure 3, but shown with thick lines). Two simulated energy spectra of downgoing protons from all proton populations are also represented for comparison. We have used the "fast SW" simulation. To obtain the simulated energy spectra, the proton fluxes were averaged over time for two time intervals to obtain a magnetosheath energy spectrum (from 19:45 UT to 19:49 UT, thin red line) and a precipitating proton energy spectrum "below the IMB" (from 19:36 UT to 19:41 UT, thin blue line).

[52] The simulated energy spectra are thermalized and heated. There is no evident energy peak in both simulated spectra. According to the simulation, the overall flux in the magnetosheath is larger than the flux below the IMB. The flux difference is larger at 100 eV than at 10 keV because the magnetic field in the pile-up region deflects low energy protons more effectively.

[53] The observed and simulated spectra in the magnetosheath agree well for energies >2 keV. The energy ranges of the observed and simulated precipitating protons below the IMB also reasonably agree between 1 and 3 keV, although the observations show higher fluxes beyond 3 keV. The absence of low energy protons in the observed spectra is an instrumental effect. As noted above, in the operation mode in question the IMA low energy cutoff was 700 eV (see the dashed vertical line). Since May 2007, the energy range of IMA is extended down to 10 eV, which enables the observations of low-energy (<50 eV) protons when the instrument is run in the high post-acceleration mode [*Lundin et al.*, 2009].

5. Discussion and Conclusion

[54] The main reason for proton precipitation is the large gyroradius of the hot magnetosheath protons relative to the size of the induced magnetosphere in the subsolar region. The temperature of the shocked plasma near the subsolar point is 400–600 eV [*Lundin et al.*, 1993]. Therefore, fluxes of protons with energy up to a few keV are still significant. The gyroradius of the 1–5 keV heated protons in a magnetic field of 50 nT (value in the subsolar magnetic pile-up region) is ~100–200 km. The height of the IMB is ~393 km at 7° SZA and the height of the PEB is ~352 km at 6° SZA (Figure 1). This result implies that the thickness of the subsolar magnetic pile-up region is about 40 km between 6°–7° SZA during the time of our observations. This thickness is smaller than the proton gyroradius previously calculated. Therefore, protons of a few keV may reach altitudes down to 200–300 km between 6°–7° SZA. This result is in reasonable agreement with the observations (scan 5 in the same SZA range).

[55] Figure 1 indicates a change in the proton energy spectrum when altitude decreases. When the IMB is crossed inward, the proton energy spectrum becomes narrower in energy, the fluxes decrease, and the low-energy component of the energy spectrum disappears: the original magnetosheath energy spectrum is strongly disturbed by the penetration through the IMB. For instance, in scans 1 and 2, the energy range is 1–4 keV, while for scan 4 (at pericenter), the protons have higher energies: 4–5 keV. The same change in the energy spectrum is also visible when comparing the proton energy distribution in scan 5 to the distribution during 19:46 UT–19:49 UT. The high-energy protons penetrate deeper than the low-energy protons due to a larger gyroradius in the pile-up region.

[56] The proton fluxes in scan 3–4 have a very narrow energy distribution, which suggests they may be pick-up protons precipitating. On the other hand, the solar wind alpha particles are observed to precipitate into the Martian atmosphere with narrow energy distributions [*Stenberg et al.*, 2011], like the precipitating protons. Hence, we argue that the observed protons can be of solar wind origin.

The observation cannot separate between the planetary protons and the solar wind protons but the model suggests that the observed precipitating protons originate both from the exosphere and the solar wind.

[57] In addition, one might remark that the high energy component in the last proton scan in Figure 1d (the red spot at energy ≥5 keV at 19:54 UT–19:55 UT) looks like the fluxes in scans 3–4. This red spot corresponds to alpha particles contaminating the measurement.

[58] The simulations (see Figure 7) indicate that the precipitating proton flux decreases more at lower energies than at higher energies when the altitude decreases. However, the decrease at low energies is not as sharp as in the observations: we measure only protons with energies ≥4 keV in scans 3 and 4 around the pericenter. It is possible that the protons are observed at the lowest altitude with a significant flux because of a transient increase in the magnetosheath proton temperature. A higher proton temperature can result in protons with higher energies and larger gyroradii. These protons with large gyroradii would pass through the IMB and penetrate deep into the atmosphere, which is consistent with the observations in scans 3–4.

[59] When searching for an orbit suitable for a case study of the proton precipitation, we noticed that the precipitation was not observed for all orbits investigated. This suggests that the precipitation is a transient phenomenon. It is possible that no proton penetration would have been measured at the pericenter if the precipitation was not enhanced by a change in the magnetosheath conditions.

[60] When the precipitating protons reach the exobase, the cascade of CX reactions and elastic and non-elastic collisions occurs, and a fraction of the precipitating proton flux may be backscattered and leave the system as energetic hydrogen atoms (ENAs) [*Kallio and Barabash*, 2001; *Shematovich et al.*, 2011]. *Shematovich et al.* [2011] investigated the transport of precipitating protons into the Martian atmosphere using a Direct Monte Carlo (DMC) model, and showed that, when no magnetic field is present, 8% of the incident energy proton flux is backscattered by the Martian atmosphere as upgoing hydrogen energy flux. If the measured precipitating protons (10^8–10^9 eV cm^{-2} s^{-1}) are reflected back as ENAs, an ENA flux of 10^7–10^8 eV cm^{-2} s^{-1} is expected. *Futaana et al.* [2006] observed hydrogen ENAs emitted from the dayside of Mars at low (∼600 km) altitude on the same day (27 February 2004) as the proton observations considered in this paper. They reported fluxes of ∼1 keV hydrogen atoms to be 10^7 H$^+$ cm^{-2} s^{-1}, corresponding to energy fluxes of 10^{10} eV cm^{-2} s^{-1}, i.e., 100–1000 times higher than the backscattered ENA energy flux that might have been associated with the proton precipitation. Therefore, the main source of the dayside ENAs is unlikely to be the precipitating protons.

[61] To understand the gross effect of proton precipitation onto the atmosphere we first estimate the maximal horizontal extent of proton precipitation along the orbit. The spacecraft velocity close to the pericenter is ∼4 km s^{-1}. With the elevation scans 1–5 (192 s each), we obtain a spatial extent of ∼4000 km along the orbit if we assume a stationary precipitation during this orbit.

[62] The heating due to proton precipitation can be compared to solar heating. The energy flux associated with the solar Extreme Ultraviolet (EUV) radiation absorption for the altitude range of 100–240 km is $1.4 \cdot 10^{11}$ eV cm^{-2} s^{-1} [*Kallio et al.*, 1997], which is ∼20 times greater than the observed maximal precipitation energy flux value ($7 \cdot 10^9$ eV cm^{-2} s^{-1}, in bold in Table 1), i.e., proton precipitation is not a significant heating source for the dayside atmosphere.

[63] In summary, due to the small size of the subsolar magnetosheath and the high plasma temperature, protons with a few keV energies and large gyroradius may reach the upper atmosphere. The hybrid simulation shows that both the shocked solar wind protons and the planetary picked-up protons contribute to the observed precipitation, with a larger contribution coming from the solar wind protons. The observations indicate that the flux of the low-energy protons is more reduced that the flux of the higher-energy protons when the altitude decreases, which is consistent with the gyroradius effect. Nevertheless, this result is less evident in the model. A fast solar wind stream can explain the high energies of the precipitating protons observed on 27 February 2004. Proton precipitation can occur on a scale of few thousands kilometers along the orbit. The precipitation occurs intermittently and it may be triggered by the transient changes in the magnetosheath temperature. The study of more precipitation events is needed to clarify the relationship between the magnetic anomalies and the precipitation. The energy flux of the precipitating protons (10^8–10^9 eV cm^{-2} s^{-1}) is much smaller than the solar UV energy flux onto the upper atmosphere.

[64] Future work will be a statistical study of the observed proton fluxes to investigate the influence of the solar wind conditions, the solar wind convection electric field and the magnetic anomalies on proton precipitation.

[65] **Acknowledgments.** C. Diéval acknowledges funding from the Kungliga Vetenskapsakademien. C. Diéval and G. Stenberg were supported by the National Graduate School of Space Technology of the Luleå Technical University. The Swedish contribution to the ASPERA-3 experiment was supported by the Swedish National Space Board. The authors acknowledge E. Penou at the Centre d'Etude Spatiale des Rayonnements (France) for providing the data analysis software CL and D. H. Hurley at the Johns Hopkins University Applied Physics Laboratory (USA) for providing upstream dynamic pressure proxy data. The authors also acknowledge Arnaud Valeille, University of Michigan, for providing the hot hydrogen and hot oxygen profiles used in the hybrid model. The authors thank the anonymous reviewers for their help in improving the paper.

[66] Masaki Fujimoto thanks the reviewers for their assistance in evaluating this paper.

References

Acuña, M. H., et al. (1998), Magnetic field and plasma observations at Mars: Preliminary results of the Mars Global Surveyor Mission, *Science*, *279*(5357), 1676–1680, doi:10.1126/science.279.5357.1676.

Acuña, M. H., et al. (1999), Global distribution of crustal magnetization discovered by the Mars Global Surveyor MAG/ER experiment, *Science*, *284*(5415), 790–793, doi:10.1126/science.284.5415.790.

Barabash, S., et al. (2006), The Analyzer of Space Plasmas and Energetic Atoms (ASPERA-3) for the Mars Express mission, *Space Sci. Rev.*, *126*(1–4), 113–164, doi:10.1007/s11214-006-9124-8.

Brain, D. A., et al. (2005), Variability of the altitude of the Martian sheath, *Geophys. Res. Lett.*, *32*, L18203, doi:10.1029/2005GL023126.

Brain, D. A., et al. (2010), A comparison of global models for the solar wind interaction with Mars, *Icarus*, *206*(1), 139–151, doi:10.1016/j.icarus.2009.06.030.

Brecht, S. H. (1997), Solar wind proton deposition into the Martian atmosphere, *J. Geophys. Res.*, *102*(A6), 11,287–11,294, doi:10.1029/97JA00561.

Cain, J. C., et al. (2003), An n = 90 internal potential function of the Martian crustal magnetic field, *J. Geophys. Res.*, *108*(E2), 5008, doi:10.1029/2000JE001487.

Chaufray, J. Y., et al. (2008), Observation of the hydrogen corona with SPICAM on Mars Express, *Icarus*, *195*(2), 598–613, doi:10.1016/j.icarus.2008.01.009.

Crider, D. H., et al. (2003), A proxy for determining solar wind dynamic pressure at Mars using Mars Global Surveyor data, *J. Geophys. Res.*, *108*(A12), 1461, doi:10.1029/2003JA009875.

Dubinin, E., et al. (2008), Structure and dynamics of the solar wind/ionosphere interface on Mars: MEX-ASPERA-3 and MEX-MARSIS observations, *Geophys. Res. Lett.*, *35*, L11103, doi:10.1029/2008GL033730.

Fedorov, A., et al. (2006), Structure of the Martian wake, *Icarus*, *182*(2), 329–336, doi:10.1016/j.icarus.2005.09.021.

Frahm, R. A., et al. (2006), Carbon dioxide photoelectron energy peaks at Mars, *Icarus*, *182*(2), 371–382, doi:10.1016/j.icarus.2006.01.014.

Fränz, M., et al. (2006), Plasma intrusion above Mars crustal fields—Mars Express ASPERA-3 observations, *Icarus*, *182*(2), 406–412, doi:10.1016/j.icarus.2005.11.016.

Fulle, M., et al. (2007), Discovery of the atomic iron tail of comet McNaught using the heliospheric imager on STEREO, *Astrophys. J.*, *661*, L93–L96, doi:10.1086/518719.

Futaana, Y., et al. (2006), First ENA observations at Mars: ENA emissions from the Martian upper atmosphere, *Icarus*, *182*(2), 424–430, doi:10.1016/j.icarus.2005.09.019.

Kallio, E., and S. Barabash (2001), Atmospheric effects of precipitation energetic hydrogen atoms on the Martian atmosphere, *J. Geophys. Res.*, *106*(A1), 165–177, doi:10.1029/2000JA002003.

Kallio, E., and P. Janhunen (2001), Atmospheric effects of proton precipitation in the Martian atmosphere and its connection to the Mars-solar wind interaction, *J. Geophys. Res.*, *106*(A4), 5617–5634, doi:10.1029/2000JA000239.

Kallio, E., and P. Janhunen (2003), Modeling the solar wind interaction with Mercury by a quasineutral hybrid model, *Ann. Geophys.*, *21*(11), 2133–2145, doi:10.5194/angeo-21-2133-2003.

Kallio, E., et al. (1997), Charge exchange near Mars: The solar wind absorption and energetic neutral atom production, *J. Geophys. Res.*, *102*(A10), 22,183–22,197, doi:10.1029/97JA01662.

Kallio, E., et al. (2008), On the properties of O^+ and O_2^+ ions in a hybrid model and in Mars Express IMA/ASPERA-3 data: A case study, *Planet. Space Sci.*, *56*, 1204–1213, doi:10.1016/j.pss.2008.03.007.

Kallio, E., et al. (2010), Oxygen ion escape at Mars in a hybrid model: High energy and low energy ions, *Icarus*, *206*, 152–163, doi:10.1016/j.icarus.2009.05.015.

Lundin, R., et al. (1993), *Plasma Environment of Non-Magnetic Planets*, edited by T. Gombosi, 311 pp., Pergamon, New York.

Lundin, R., et al. (2004), Solar wind-induced atmospheric erosion at Mars: First results from ASPERA-3 on Mars Express, *Science*, *305*(5692), 1933–1936, doi:10.1126/science.1101860.

Lundin, R., et al. (2008), A comet-like escape of ionospheric plasma from Mars, *Geophys. Res. Lett.*, *35*, L18203, doi:10.1029/2008GL034811.

Lundin, R., et al. (2009), Atmospheric origin of cold ion escape from Mars, *Geophys. Res. Lett.*, *36*, L17202, doi:10.1029/2009GL039341.

Ma, Y., et al. (2004), Three-dimensional, multispecies, high spatial resolution MHD studies of the solar wind interaction with Mars, *J. Geophys. Res.*, *109*, A07211, doi:10.1029/2003JA010367.

Mitchell, D. L., et al. (2001), Probing Mars' crustal magnetic field and ionosphere with the MGS Electron Reflectometer, *J. Geophys. Res.*, *106*(E10), 23,419–23,427, doi:10.1029/2000JE001435.

Nagy, A. F., et al. (2004), The plasma environment of Mars, *Space Sci. Rev.*, *111*, 33–114, doi:10.1023/B:SPAC.0000032718.47512.92.

Shematovich, V. I., et al. (2011), Protons and hydrogen atoms transport in the Martian upper atmosphere with an induced magnetic field, *J. Geophys. Res.*, *116*, A11320, doi:10.1029/2011JA017007.

Soobiah, Y., et al. (2006), Observations of magnetic anomaly signatures in Mars Express ASPERA-3 ELS data, *Icarus*, *182*(2), 396–405, doi:10.1016/j.icarus.2005.10.034.

Stenberg, G., et al. (2011), Observational evidence of alpha particle capture at Mars, *Geophys. Res. Lett.*, *38*, L09101, doi:10.1029/2011GL047155.